

Article

Effect of Eccentric Tension on the Response of Wrinkle Defects in Carbon Fiber-Reinforced Composite Laminates

Li Ma ^{1,2,*}, Kaidi Ying ¹ , Ange Wen ², Jing Guo ¹ and Jinyang Zheng ²¹ Institute of Applied Mechanics, Zhejiang University of Technology, Hangzhou 310018, China² Institute of Process Equipment, Zhejiang University, Hangzhou 310027, China

* Correspondence: malizjut@zjut.edu.cn

Abstract: Composite pressure vessels (CPVs) have become the main equipment for hydrogen storage; however, the effect of defect in the laminates of CPVs is difficult to detect. In this paper, composite specimens containing wrinkle defects were investigated, and a heterogeneity model of a wrinkle defect is proposed. A three-dimensional finite element code was developed to predict the behavior of carbon fiber-reinforced composite laminates with wrinkle defects. The effect of the geometric asymmetry of clamping was distinguished from the whole response. It was found that wrinkle defects are sensitive to tension but completely insensitive to torsion and that the distortion of out-of-plane displacement is strongly dependent upon wrinkle defects. An optical–mechanical method based on fringe projection was presented to measure the response of wrinkle defects, which shows an outstanding performance on wrinkle location and deformation visualization.

Keywords: fiber-reinforced composite laminates; wrinkle defects; fringe projection; optical–mechanical method



Citation: Ma, L.; Ying, K.; Wen, A.; Guo, J.; Zheng, J. Effect of Eccentric Tension on the Response of Wrinkle Defects in Carbon Fiber-Reinforced Composite Laminates. *Energies* **2023**, *16*, 209. <https://doi.org/10.3390/en16010209>

Academic Editor: Vladislav A. Sadykov

Received: 25 November 2022

Revised: 22 December 2022

Accepted: 23 December 2022

Published: 25 December 2022



Copyright: © 2022 by the authors. Licensee MDPI, Basel, Switzerland. This article is an open access article distributed under the terms and conditions of the Creative Commons Attribution (CC BY) license (<https://creativecommons.org/licenses/by/4.0/>).

1. Introduction

Composite pressure vessels (CPVs) are important pieces of equipment for hydrogen storage. However, defects in CPVs will inevitably occur during the manufacturing process, leading to the reduction in fatigue life and degradation in strength.

Wave defects, also known as misalignment in the form of in-plane waviness and out-of-plane wrinkling, are frequently encountered flaws in fiber-reinforced composite structures. Such defects commonly arise from manufacturing processes, i.e., the hot drape forming (HDF) process [1–3] and Liquid Composite Molding (LCM) processes such as Resin Transfer Molding (RTM) [4,5].

Factors such as the local fiber compressive stresses [6], stacking layup sequences [6,7], part thickness, geometry, and tool–part interactions [8] contribute to the formation of wrinkles.

Figure 1 [9] shows an example of a wrinkle defect on a CPV, where circumferential layers were locally squished by a subsequently wound helical layer with a lagging pattern, which further leads to the local accumulation of wrinkled material. In consequence, these defects may potentially trigger a preliminary vessel failure.

Compressive properties are more sensitive to out-of-plane wrinkling [10–12], among which a 33.0% reduction in compressive strength has been reported [12]. Tension failure [13,14], as well as tension–tension cyclic behavior [15,16], has been studied, where small delamination can be initiated early during the load history and grow steadily with an increasing number of cycles.

Usually, the shape and size of a wrinkle can be described as, e.g., a bell-shaped curve of a Gaussian function [16] or sine/cosine functions. Further observations found that the wavelength, amplitude, and deflection angles of wrinkles are approximately normally distribution or have a Weibull distribution [17], and probabilistic models were developed accordingly to assess the reliability of wind blades with such defects [18].

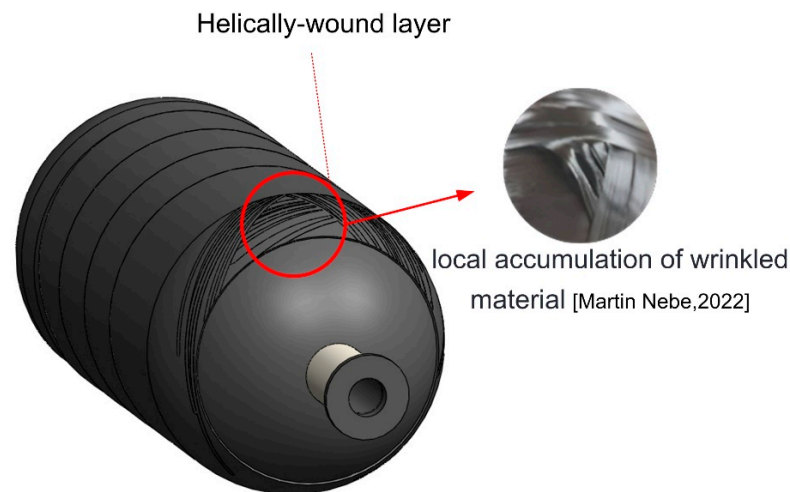


Figure 1. Example of a manufacturing wrinkle defect [9].

These methods of observing wrinkles are also nondestructive testing (NDT) methods. An ultrasonic array technique is used to detect the fiber waviness [19], and based on the ultrasonic pulse-echo technique, both in-plane waviness and out-of-plane wrinkling were visualized [20–22]. The other imaging techniques include laser-ultrasound (LU) [23] and microwave scanning [24].

The microscopic images capturing out-of-plane defect height, type, and location were obtained by using micro-computational tomography (CT) [1]. This method employs multiple field image analysis (MFIA) [25] to visualize the microscopic characteristic of waviness. However, CT scans are not feasible in industry practice because of their huge cost and risk of radioactive contamination.

On the other hand, optical-mechanical methods such as Digital Image Correlation (DIC) provide an approach to visualize deformation that shows highly localized concentrations surrounding the wrinkle [13,26]. Here, the concentrated deformation not only indicates the location of defects but also gives an assessment of the performance of defective structures.

In order to observe the wrinkles' effects on CPVs in the future, we carried out a preliminary study on the composite laminates and proposed a fringe projection method to assess the wrinkle defects by measuring the abnormal response of displacement.

The paper is organized as follows: Firstly, a heterogeneity model to describe the probability distribution of wrinkles is presented, which is then implanted in the finite element code to predict the structural response. The additional moments induced by eccentric tension are considered. Then, the specimens containing a deterministic wrinkle are investigated using the fringe projection method, and error analysis is also conducted.

2. Micro-Mechanical Model of Wrinkles

2.1. Wrinkle in Laminate

The wrinkle geometry is usually described as uniform or linear gradient [27]. This work mainly considered wrinkles occurring in thin laminate, since their thicknesses are very small and the variation along the height direction is limited; thus, the wrinkles are assumed to be uniform.

Figure 2 shows an idealized model of a uniform wrinkle, where all fibers undulate with an identical cosine waveform and are parallel to each other within the wrinkle region. The profile of a uniform wrinkle is described by the following Equation (1):

$$z(x) = z_0 + A \cos\left(\frac{2\pi x}{\lambda}\right), \quad |x| \leq \lambda/2 \quad (1)$$

where x is the longitudinal direction parallel to the fiber direction, $z(x)$ is the coordinate through-thickness direction, and z_0 is the corresponding value in a wrinkle-free flat laminate. A and λ are the maximum amplitude and wavelength of the wrinkle, respectively.

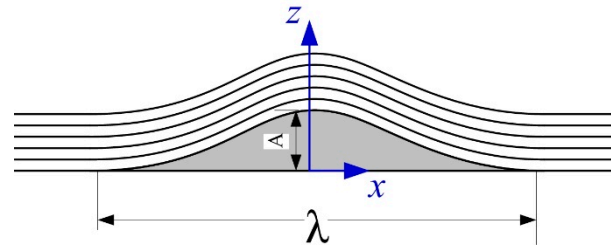


Figure 2. Uniform wrinkle model.

2.2. Effective Stiffness

Figure 3 shows the two-step homogenization technique used to estimate the effective elastic properties of wrinkled laminate. Firstly, the represented volume element (RVE) containing a wrinkle was taken as a wrinkle-free laminate to conduct the vertical homogenization (see Figure 3b). In the second step, imaging of the bent fibers and their horizontal homogenization was conducted (see Figure 3c). Such two-step homogenization is only applicable to uniform wrinkles, and the detailed homogenization process is listed in Appendix A, which also can be referenced in [27–30].

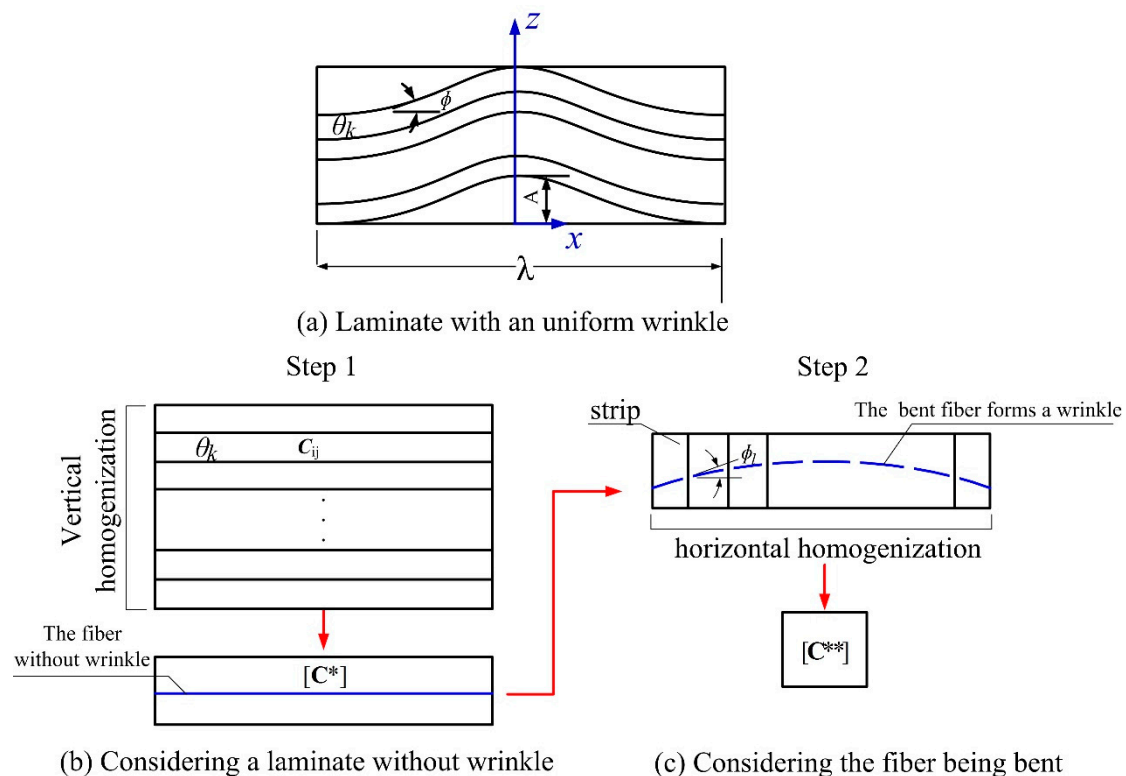


Figure 3. Two-step homogenization procedure for uniform wrinkle.

3. Structural Response with Wrinkles

In response measurements of wrinkled laminate, it should be noticed that the geometric asymmetry of the clamping may lead to additional moments, which have an overall impact on the structure response and may obscure the true response of the defect. Thus, a heterogeneous wrinkle model with random distribution is necessary.

3.1. Heterogeneity Model

According to [17,18,25,31], it is rational to presume that the wrinkle ratio of A and λ obeys the normal distribution and has the following form:

$$F(\gamma) = \frac{1}{\sqrt{2\pi}S} \exp\left[-\frac{(\gamma - \gamma_0)^2}{2S^2}\right] \quad (2)$$

where γ is the wrinkle ratio, γ_0 denotes the average value of ratio, and S is the standard deviation. Considering the wrinkle towards up or down, the average ratio of the wrinkle's shape is zero.

3.2. Heterogeneity Model Implanted in FEA

The normal size distribution of the defects, as well as the random distribution of their locations, is considered together, as shown in Figure 4.

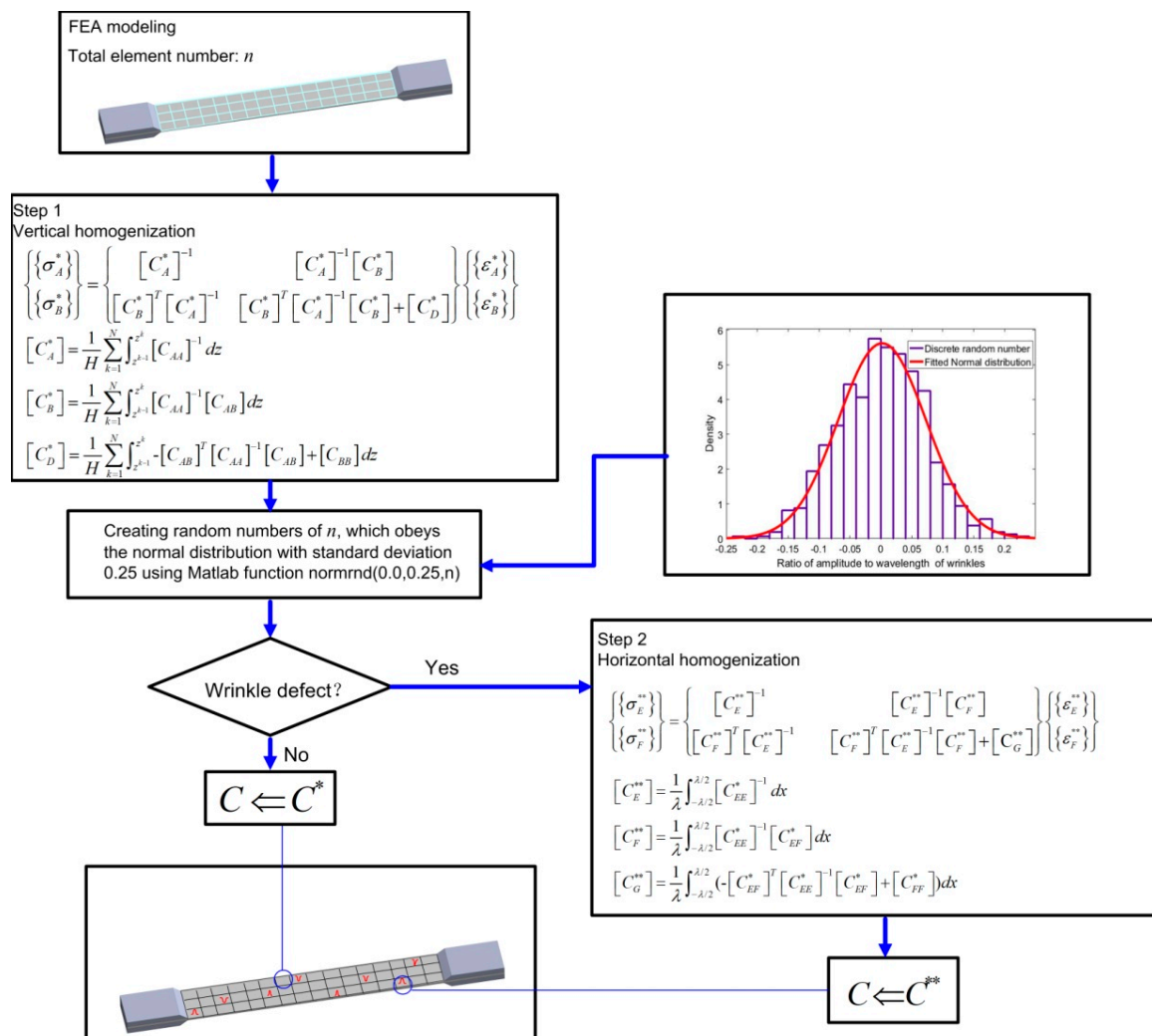


Figure 4. Wrinkle defects implanted in structure *: the equations can be referenced in Appendix A.

A normal distribution function is designed to obtain a wrinkle ratio between 0 and 0.25. In the finite element (FE) model, the wrinkle defect is regarded as a disturbance to the stiffness matrix of each element. The degree of this disturbance depends on the value of the wrinkle ratio. If the ratio is zero, the stiffness of the element reflects that of idealized laminate. In this way, the heterogeneity model was implanted in finite element analysis (FEA), and the behavior of a structure with randomly distributed wrinkles can be predicted.

The numerical simulation considering the heterogeneity model was conducted by “Magic matrix”, which is a program developed by our research group, based on MATLAB R2016a.

3.3. Structural Response

Figure 5a shows the idealized laminate model with a stacking sequence $(0,90,0,90)_s$. The length and the width are 250 mm and 25 mm, respectively, and the thickness is 0.8 mm. The global Cartesian coordinate is displayed using an x - y - z system. The bottom of the laminate is constrained, and the tensile load was applied on the top end.

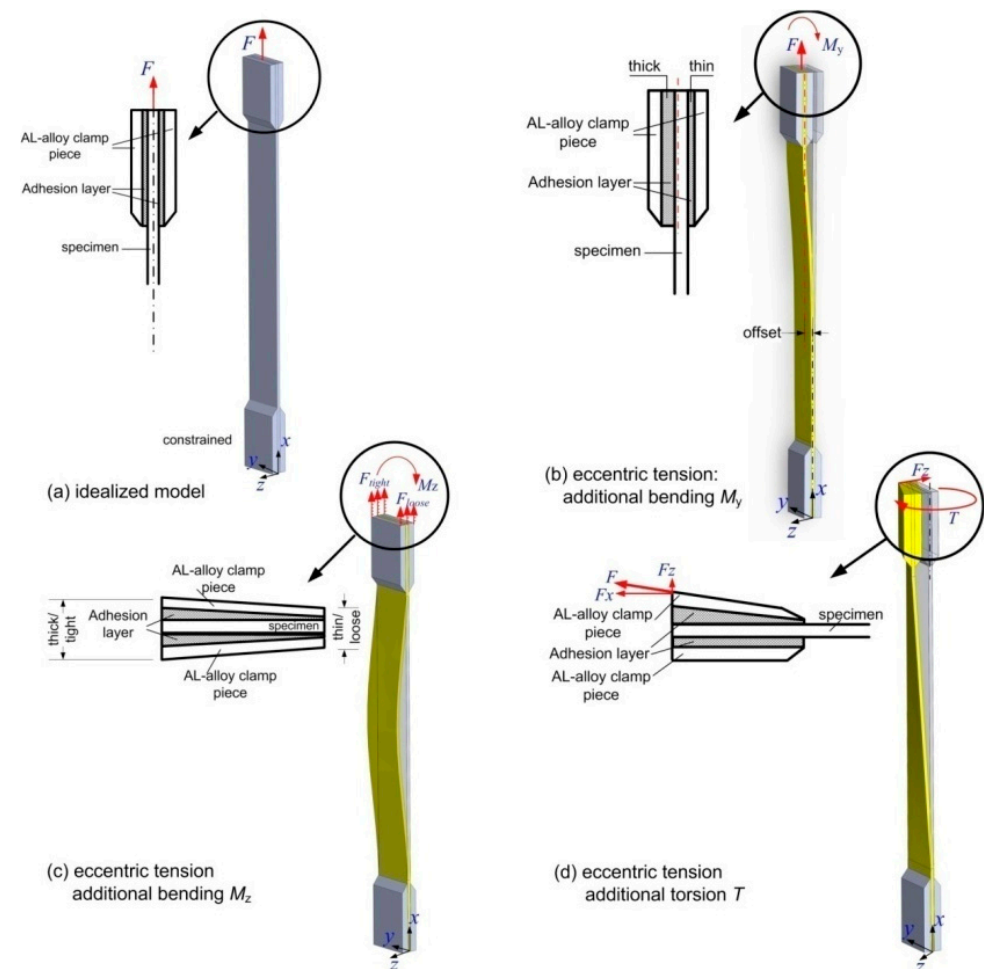


Figure 5. Additional bending and torsion moments along with tensile load.

Since the laminates are very thin, the different thickness of the adhesion layer has a great influence on geometric symmetry of clamps during the preparation of the specimens. In comparison with the idealized model (Figure 5a), some additional bending and torsion moments may be caused by eccentric tension; see Figure 5b–d.

The mechanical properties of the orthotropic laminate are listed in Table 1.

Table 1. Mechanical properties of orthotropic laminate.

E_{11} (GPa)	E_{22}/E_{33} (GPa)	G_{12} (GPa)	G_{23} (GPa)	G_{31} (GPa)	ν_{21}	ν_{32}	ν_{31}
133.3	9.09	7.23	3.16	7.24	0.261	0.436	0.261

3.3.1. Tension

Figure 6 shows the displacement responses of the laminate under tensile load. The in-plane displacements along the x and y directions are u and v , respectively, and are represented by contour maps; w is the out-of-plane displacement displayed by the 3D surface. No displacement distortion can be found without wrinkle defects; however, when considering the heterogeneity model of the defects, the out-of-plane displacements' distortion becomes obvious.

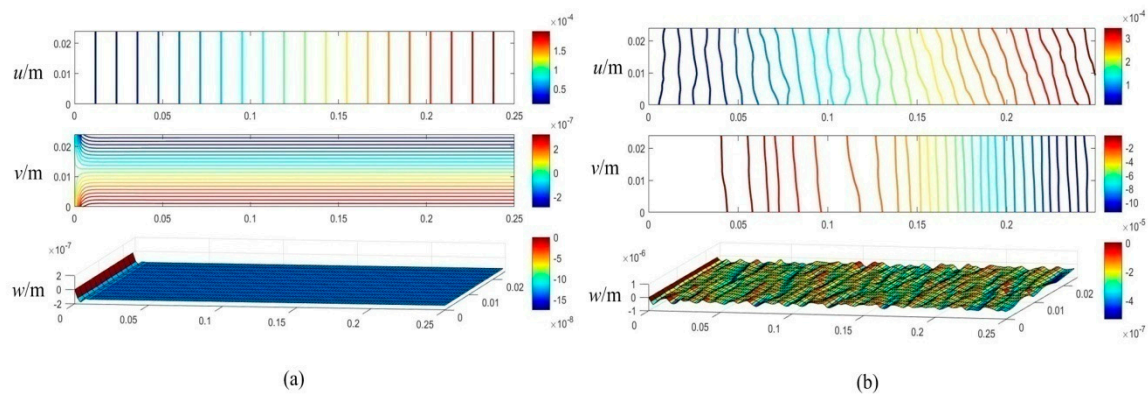


Figure 6. Structural response to tensile load (a) without wrinkles and (b) with randomly distributed wrinkles.

3.3.2. Bending around Y-Axis

Figure 7 shows the displacement response of the laminate under bending moment M_y (see Figure 5b), from which the distortion only occurred in the in-plane displacement along the y -direction when wrinkle model is considered.

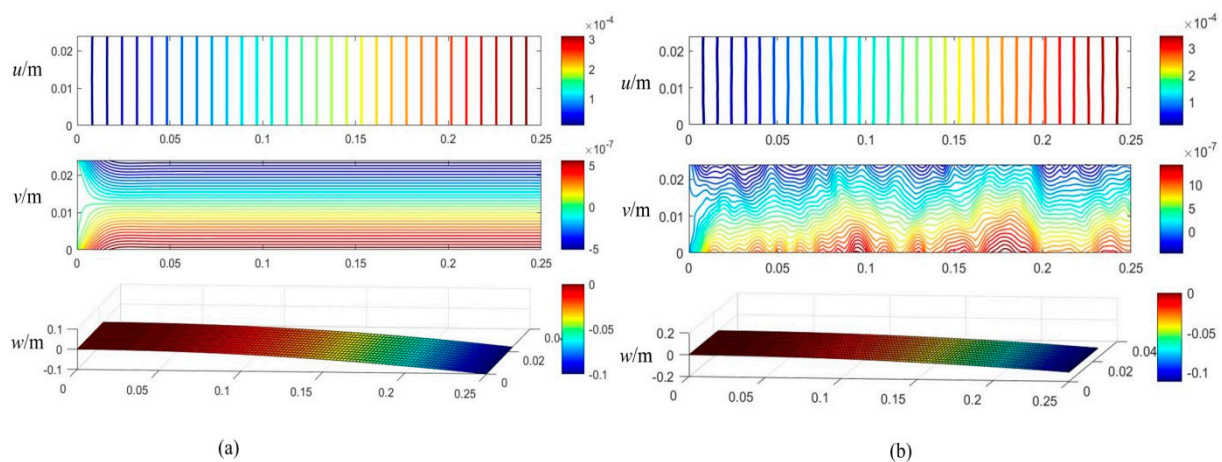


Figure 7. Structural response with bending moment M_y (a) without wrinkles and (b) with randomly distributed wrinkles.

3.3.3. Bending around Z-Axis

With eccentric tension, the bending moment M_z (see Figure 5c) should be considered. Figure 8 shows the out-of-plane displacement distortion that occurred in this situation in the wrinkle model. Note that in the two long sides of the specimen, one was straightened and the other was impressed with many local folds, which is a quite remarkable distortion effect in the out-of-plane displacement.

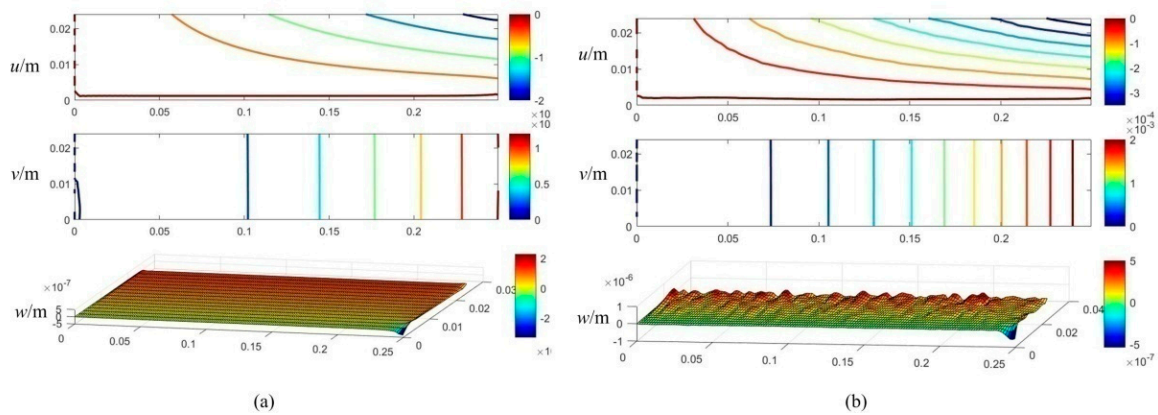


Figure 8. Structural response with bending moment M_z (a) without wrinkles and (b) with randomly distributed wrinkles.

3.3.4. Torsion

The fact that no displacement distortion was found with/without wrinkle defects under torsion moment was unexpected (see Figure 5d). Figure 9 shows that all of the displacements in the laminate remain as smooth as perfect material.

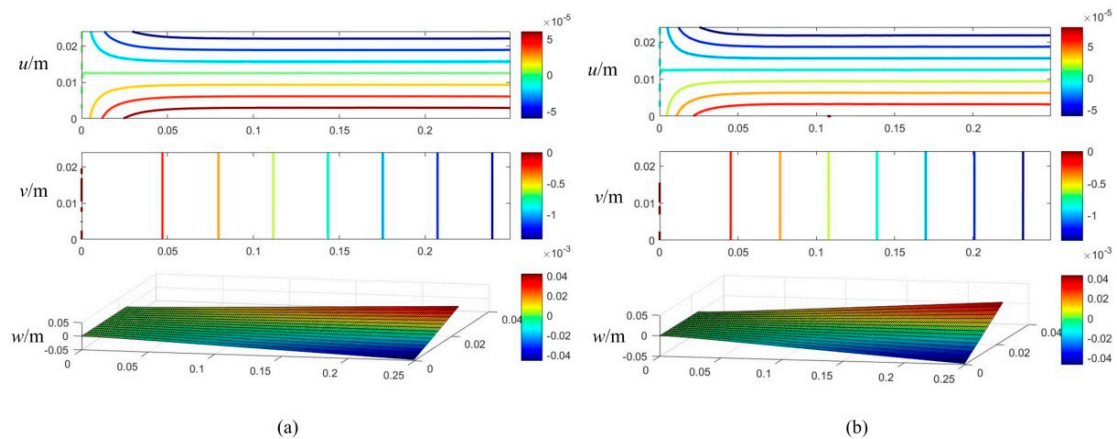


Figure 9. Structural response with torque around x-axis (a) without wrinkles and (b) with randomly distributed wrinkles.

4. Experiment Preparation

In experimental investigation, it is necessary to make a sample containing one deterministic wrinkle defect to verify the findings in Section 3.

To make sure the location of the defect has no obvious influence on the behavior of the laminate, we investigate a heterogeneity model that considers randomly distributed defects with different morphology sizes in Section 3.3. The results show that wrinkle defects always cause out-of-plane displacement distortion under tension and bending around the z-axis, regardless of where the defect is located.

4.1. Test Specimen

The specimens are made by unidirectional fiber prepreps with a thickness of 0.125 mm, a fiber mass per unit area of 100g/m², and a resin content of 20–40%. Figure 10 shows the specimens where the wrinkle defect was made in the middle of the plate, which is just for the convenience of observing the experiment.

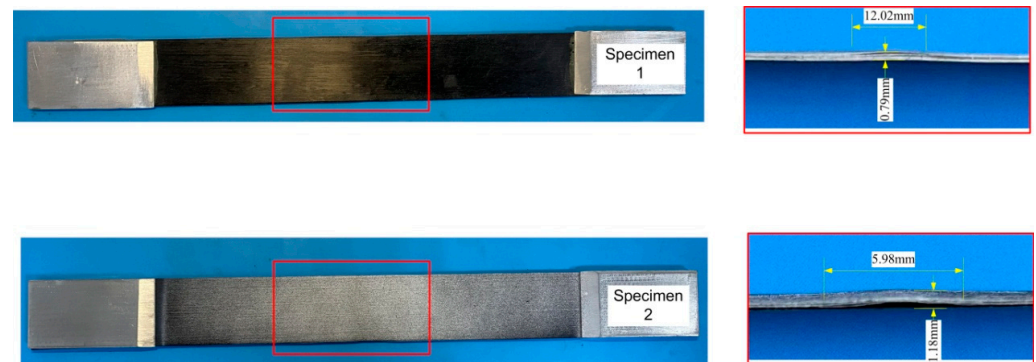


Figure 10. Morphology of wrinkles.

The geometric parameters of the wrinkles are listed in Table 2.

Table 2. Geometric parameters of wrinkle defects.

Specimen	Stacking Sequence	Wrinkle Geometry		
		λ/mm	A/mm	Waviness Ratio: A/λ
S1	[0/90/0/90] _s	12.02	0.79	0.066
S2	[0/90/0/90] _s	5.98	1.18	0.197

4.2. FEA Simulation

According to the discussion in Section 3.3, the out-of-plane displacement distortion only occurred under tension and the bending moment around the z-axis. Since the tensile test can be easily realized in the lab, tension experiments were conducted.

Firstly, FEA was used as a guide to design experimental scheme. The tension process was simulated using FE software ANSYS, Mechanical APDL 15.0, and Figure 11 shows the FEA results for specimens with and without wrinkle defects.

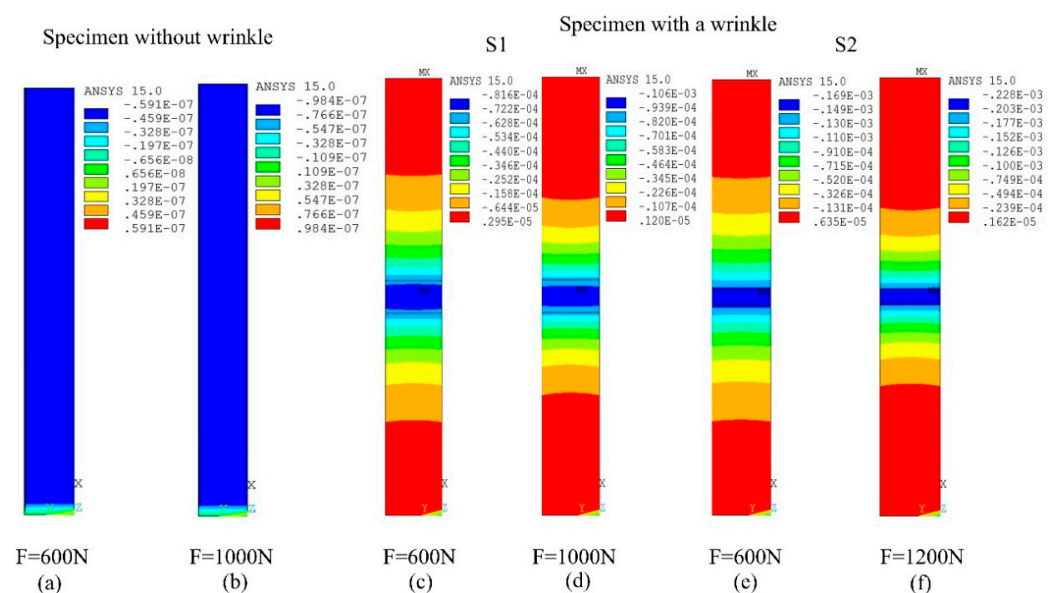


Figure 11. FEA simulation for specimens with/without wrinkle defects.

Figure 11a,b illustrate the out-of-plane displacement without defects, where the displacement field is uniformly smooth and the displacements are 0.591×10^{-4} mm and 0.984×10^{-4} mm, corresponding to tensile forces of 600 N and 1000 N, respectively.

However, when considering a wrinkle defect in the middle of the plate, the displacement distribution is greatly changed: the maximum displacements in the wrinkled zone of S1 are 0.0816 mm and 0.106 mm (see Figure 11c,d) and the maximum values of S2 are 0.169 mm and 0.228 mm (see Figure 11e,f).

It is found that the wrinkle defect causes a 10^4 amplification in out-of-plane displacement. Comparing the severity of defects, S2 (with a larger wrinkle ratio) shows a larger displacement and a narrower deformed area, which not only reflects the orientation of the wrinkles but also signifies its influence on the degradation of the material's performance.

5. Optical–Mechanical Measurement

5.1. Method

The fringe projection method has been widely used to measure three-dimensional (3D) topography. Recently, a new application including displacement and deformation measurement was developed by integrating DIC technology, where fringe projection was used for shape measurement and DIC was used for image location and matching [32,33].

However, in this paper, the fringe projection method was used independently to measure out-of-plane displacement. Figure 12 shows the experimental device and process: Firstly, the phase shift and unwrapping technology were used to obtain the 3D point clouds of laminates under different tensile forces, and then the algorithm of displacement extraction is presented in Figure 13, where the 3D topography is reconstructed by remapping and cubic spline interpolation and the out-of-plane displacement is obtained by subtracting two-point clouds.

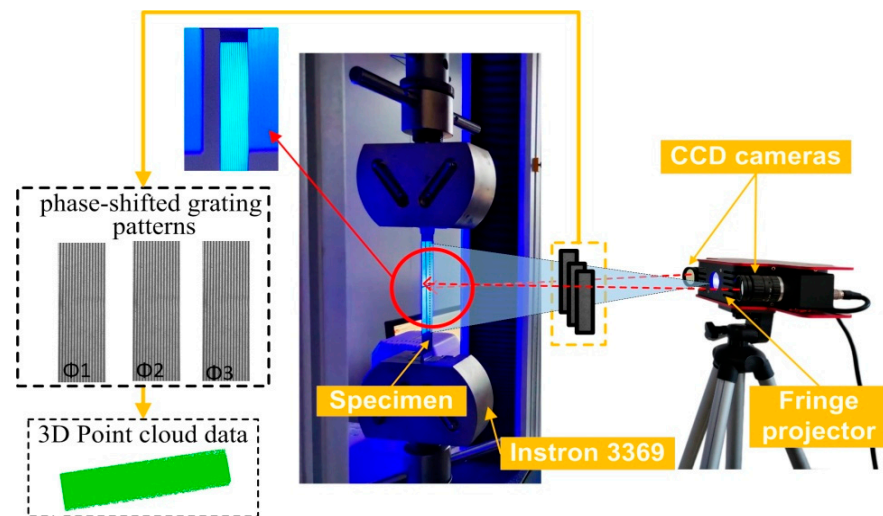


Figure 12. 3D topography measurement based on fringe projection.

5.2. Procedure

The specimen was loaded by the steps given in Table 3. The surface point cloud (also called surface depth) was measured at every load step. It was found that much better effects could be obtained by using a force of 200 N as an initial load, which is probably due to the complexity of the composites' micro-structure that the deformation changed nonlinearly from an unstressed to a forced state. Figures 14 and 15 show the measured contours of surface depths of S1 and S2, corresponding to the forces of 200 N, 800 N, and 1200 N, respectively.

Table 3. Load steps.

Specimen	Step	1	2	3
S1	Load(N)	200	800	1200
S2				

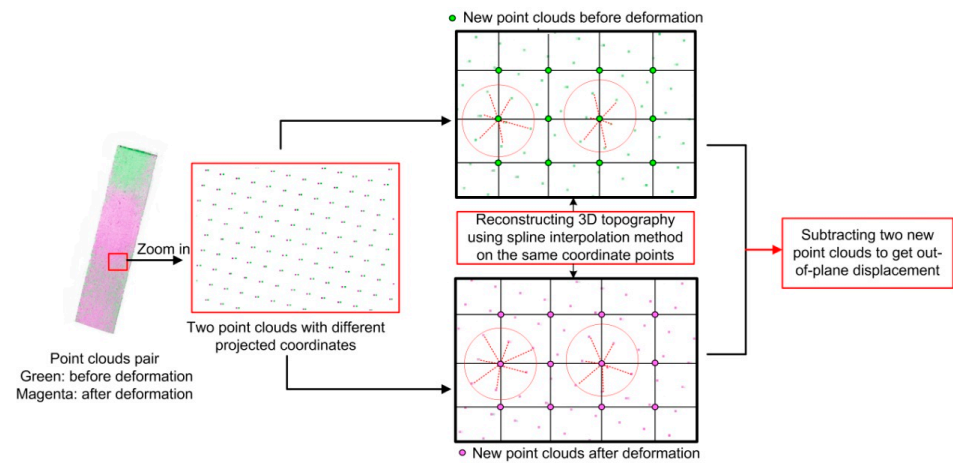


Figure 13. Displacement extraction algorithm based on 3D point clouds.

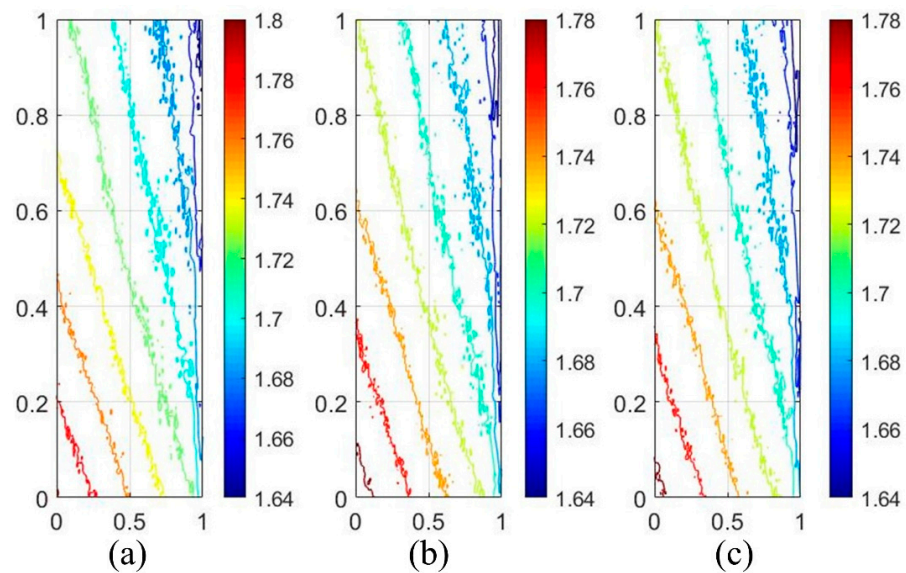


Figure 14. Depth contour of S1 (unit: cm): (a) $F = 200\text{N}$, (b) $F = 800\text{N}$, (c) $F = 1200\text{N}$.

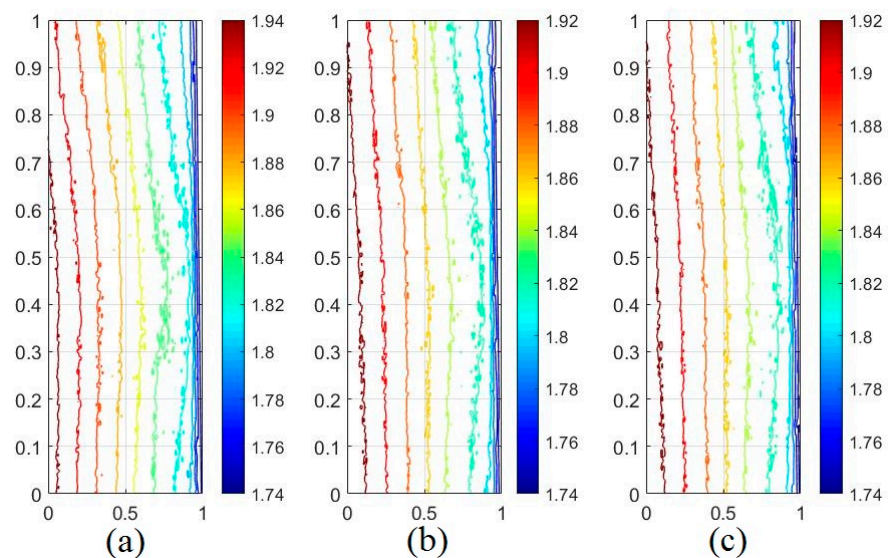


Figure 15. Depth contour of S2 (unit: cm): (a) $F = 200\text{N}$, (b) $F = 800\text{N}$, (c) $F = 1200\text{N}$.

5.3. Results Analysis

5.3.1. Out-of-Plane Displacement

Figures 16 and 17 show the out-of-plane displacement results obtained from the displacement extracting algorithm.

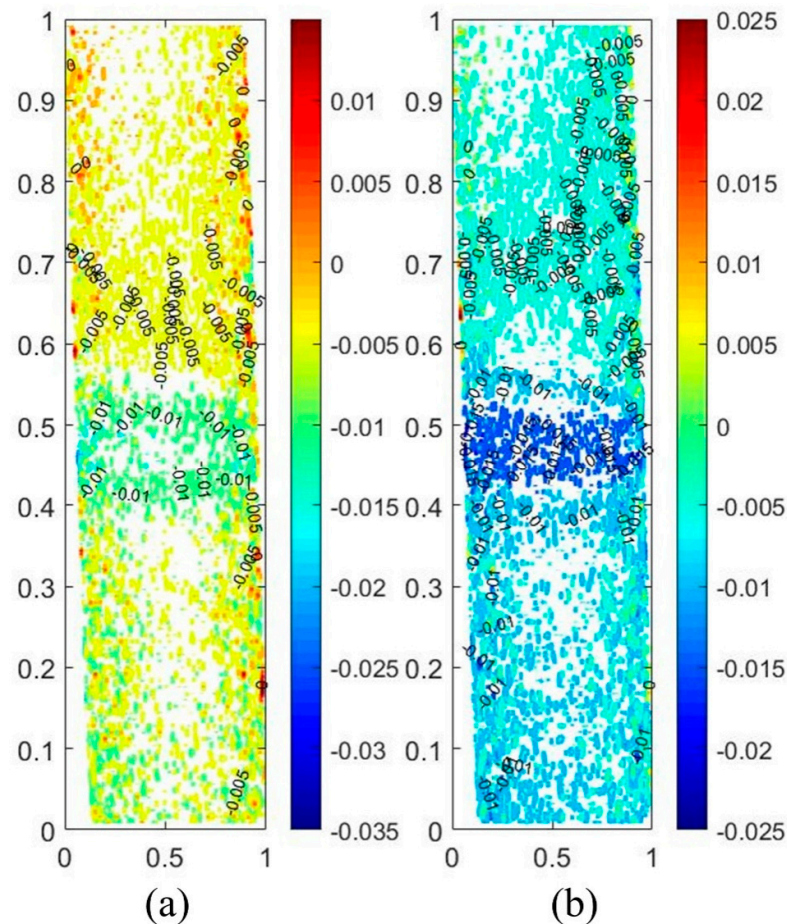


Figure 16. Out-of-plane displacement contour of S1 (unit: cm): (a) $\Delta F = 600$ N, (b) $\Delta F = 1000$ N.

As shown in Figure 16, the location of the defect can be captured well according to the out-of-plane displacement, where the measured maximum displacement is 0.100 mm for 600 N of force and 0.150 mm for 1000 N. Such a result indicates that the error compared to the FE result is 18.4% and 29.3%, respectively. Given that the true morphology of the wrinkle is not an ideal cosine function, such an error can be considered to be within an acceptable range.

Figure 17 shows the out-of-plane displacement contour of S2, where the measured displacement is concentrated in a limited area surrounding the wrinkle. The sources of errors are discussed in the next section.

5.3.2. Error Analysis

The difference between experimental and numerical results may come from two aspects:

- (1) Non-ideal cosine curves in the wrinkles in the specimen;
- (2) The additional moments introduced by geometric asymmetry.

Fortunately, according to the discussion in Section 3.3, only the bending moment around the z-axis contributes to the off-plane displacement, and its influence is discussed below.

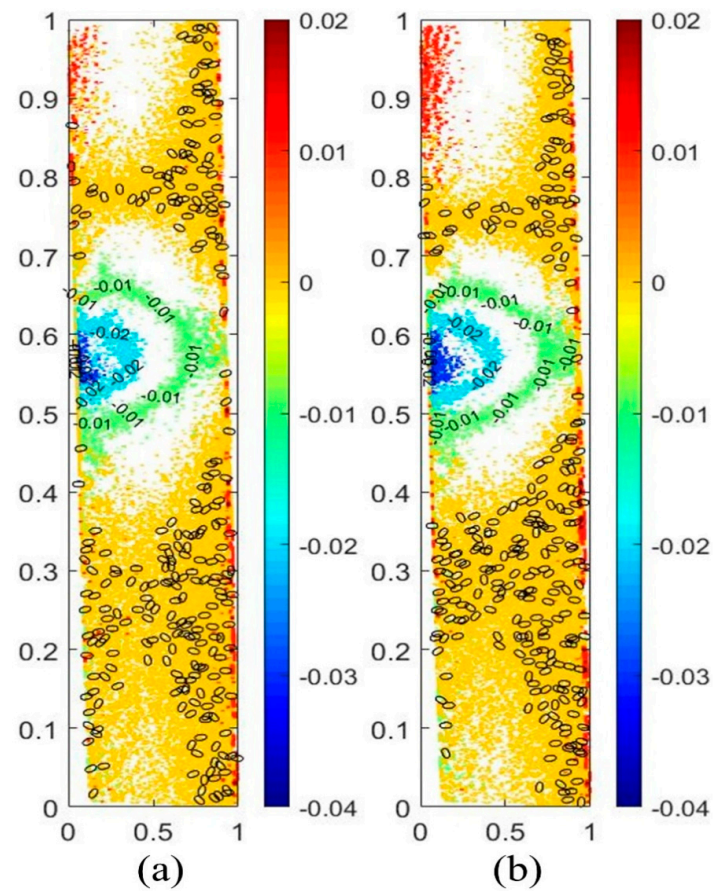


Figure 17. Out-of-plane displacement contour of S2 (unit: cm): (a) $\Delta F = 600$ N, (b) $\Delta F = 1000$ N.

Figure 18 shows the most extreme case of bending moment \bar{M}_Z . Figure 19 is the corresponding out-of-plane displacements of S2 considering the tensile load along with an additional 5~10% \bar{M}_Z in the clockwise direction, where the maximum displacements are close to 0.02 cm and 0.01 cm, which are highly consistent with the experimental results in Figure 17.

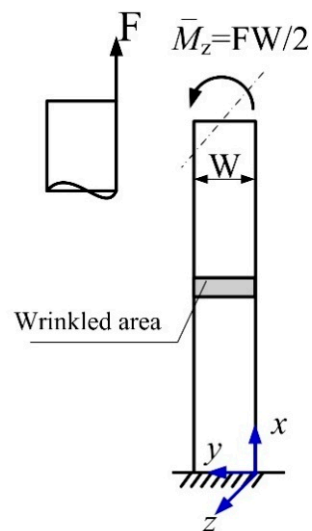


Figure 18. Additional bending moment in an extreme case.

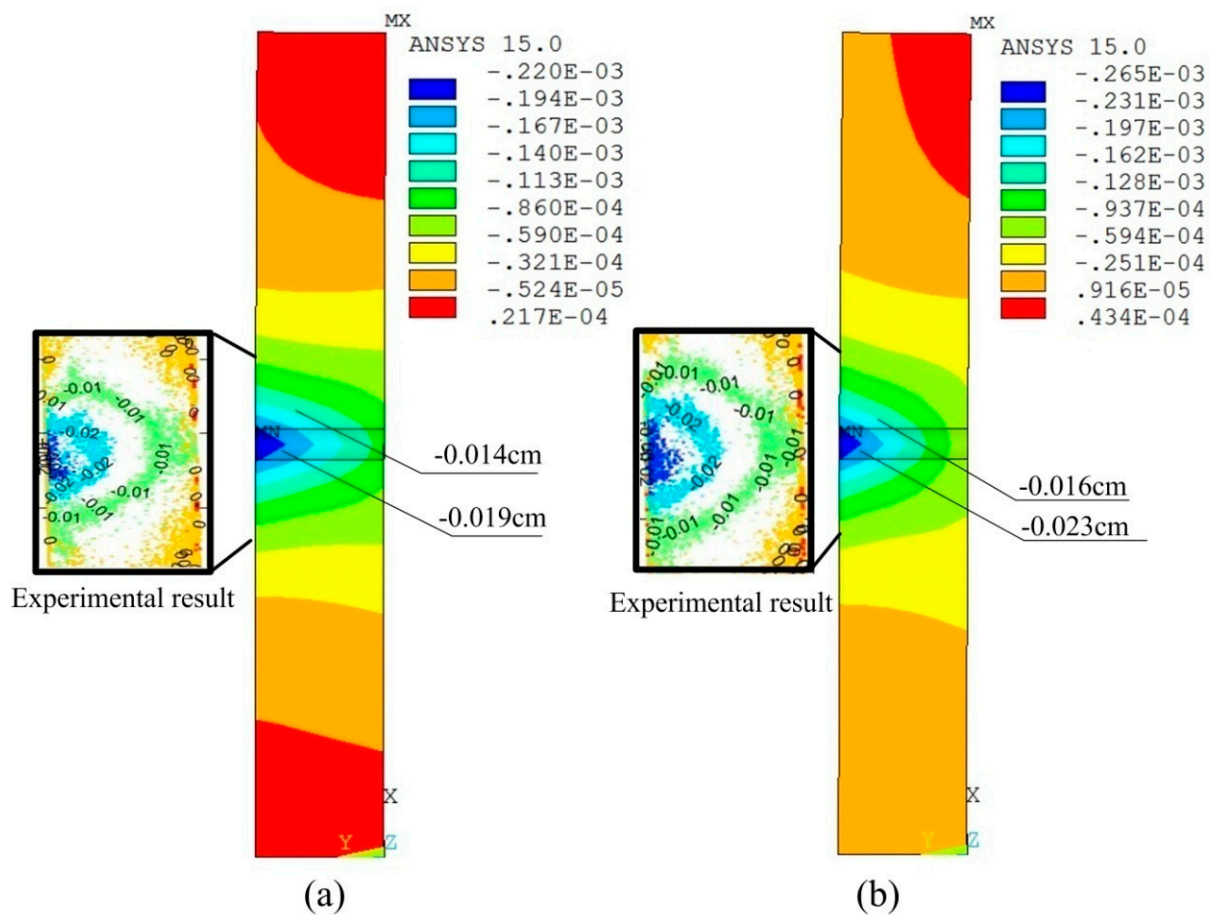


Figure 19. Out-of-plane displacement: (a) $600N + 0.05 \overline{M}_Z$, (b) $1000N + 0.10 \overline{M}_Z$.

6. Conclusions

The mechanical response to wrinkle defects, as well as the effect of geometrically asymmetric clamping, was investigated in this paper. Firstly, the heterogeneity model of the wrinkles was presented, and their behavior under different loads was numerically predicted. It was found that wrinkles are sensitive to eccentric tension and show distortion in the out-of-plane displacement.

Secondly, combined with the displacement extraction algorithm, the fringe projection technique was developed to measure the out-of-plane displacement, which exhibits an outstanding effect in wrinkle location and deformation visualization.

The method proposed in this paper is expected to be used to measure the response of wrinkle defects in laminates of CPVs.

Author Contributions: Methodology, L.M.; Validation, J.G.; Formal analysis, A.W.; Investigation, A.W.; Resources, J.Z.; Writing—original draft, L.M. and K.Y.; Visualization, K.Y.; Project administration, L.M.; Funding acquisition, L.M. All authors have read and agreed to the published version of the manuscript.

Funding: This work was supported by the National Key Research & Development Program of China (Grant No. 2021YFB4000903) and Basic Public Welfare Research Program of Zhejiang Province, China (Grant No. LGF21E040002).

Data Availability Statement: The data is not publicly available due to privacy or ethical restriction.

Conflicts of Interest: The authors declare no conflict of interest.

Appendix A

For every ply in the laminate, C'_{ij} represents the orthotropic stiffness in each ply's material coordinate system. Then, in the global coordinate system, the stiffness can be rewritten as:

$$C_{ij} = T_{\theta}^{-1} C'_{ij} T_{\theta}^{-T} \quad (A1)$$

where

$$[T_{\theta}] = \begin{bmatrix} \cos^2 \theta & \sin^2 \theta & 0 & 0 & 0 & 2 \sin \theta \cos \theta \\ \sin^2 \theta & \cos^2 \theta & 0 & 0 & 0 & -2 \sin \theta \cos \theta \\ 0 & 0 & 1 & 0 & 0 & 0 \\ 0 & 0 & 0 & \cos \theta & -\sin \theta & 0 \\ 0 & 0 & 0 & \sin \theta & \cos \theta & 0 \\ -\sin \theta \cos \theta & \sin \theta \cos \theta & 0 & 0 & 0 & \cos^2 \theta - \sin^2 \theta \end{bmatrix} \quad (A2)$$

In step 1, the laminate is taken to be wrinkle-free when conducting the vertical homogenization. It is assumed that the out-of-plane stresses σ_{zz} , τ_{yz} , τ_{zx} and in-plane strains ε_{xx} , ε_{yy} , ε_{xy} are uniform through each ply ($\sigma_{zz} = \sigma_{zz}^*$, $\tau_{yz} = \tau_{yz}^*$, $\tau_{zx} = \tau_{zx}^*$, $\varepsilon_{xx} = \varepsilon_{xx}^*$, $\varepsilon_{yy} = \varepsilon_{yy}^*$, $\varepsilon_{xy} = \varepsilon_{xy}^*$). The constitutive relation for every ply can be rewritten as:

$$\begin{Bmatrix} \{\sigma_A^*\} \\ \{\sigma_B\} \end{Bmatrix} = \begin{Bmatrix} [C_{AA}] & [C_{AB}] \\ [C_{AB}]^T & [C_{BB}] \end{Bmatrix} \begin{Bmatrix} \{\varepsilon_A\} \\ \{\varepsilon_B^*\} \end{Bmatrix} \quad (A3)$$

where the superscript * denotes the average quantities of stress and strain. The other symbols represent:

$$\begin{aligned} \{\sigma_A^*\} &= \{\sigma_{zz}^* \ \tau_{yz}^* \ \tau_{zx}^*\}^T \quad \{\sigma_B\} = \{\sigma_{xx} \ \sigma_{yy} \ \tau_{xy}\}^T \\ \{\varepsilon_A\} &= \{\varepsilon_{zz} \ \gamma_{yz} \ \gamma_{zx}\}^T \quad \{\varepsilon_B^*\} = \{\varepsilon_{xx}^* \ \varepsilon_{yy}^* \ \gamma_{xy}^*\}^T \end{aligned} \quad (A4)$$

$$[C_{AA}] = \begin{bmatrix} C_{33} & C_{34} & C_{35} \\ C_{43} & C_{44} & C_{45} \\ C_{53} & C_{54} & C_{55} \end{bmatrix} \quad [C_{AB}] = \begin{bmatrix} C_{13} & C_{23} & C_{36} \\ C_{14} & C_{24} & C_{46} \\ C_{15} & C_{25} & C_{56} \end{bmatrix} \quad [C_{BB}] = \begin{bmatrix} C_{11} & C_{12} & C_{16} \\ C_{21} & C_{22} & C_{26} \\ C_{16} & C_{26} & C_{66} \end{bmatrix} \quad (A5)$$

Equation (A3) can be turned to the following form in terms of $\{\sigma_A^*\}$ and $\{\varepsilon_B^*\}$:

$$\begin{Bmatrix} \{\varepsilon_A\} \\ \{\sigma_B\} \end{Bmatrix} = \begin{Bmatrix} [C_{AA}]^{-1} & -[C_{AA}]^{-1}[C_{AB}] \\ [C_{AB}]^T[C_{AA}]^{-1} - [C_{AB}]^T[C_{AA}]^{-1}[C_{AB}] + [C_{BB}] \end{Bmatrix} \begin{Bmatrix} \{\sigma_A^*\} \\ \{\varepsilon_B^*\} \end{Bmatrix} \quad (A6)$$

Thus, the average values of $\{\sigma_B\}$ and $\{\varepsilon_A\}$, i.e., $\{\sigma_B^*\}$ and $\{\varepsilon_A^*\}$ for a homogenized material, can be determined as:

$$\begin{Bmatrix} \{\varepsilon_A^*\} \\ \{\sigma_B^*\} \end{Bmatrix} = \begin{Bmatrix} [C_A^*] & -[C_B^*] \\ [C_B^*]^T & [C_D^*] \end{Bmatrix} \begin{Bmatrix} \{\sigma_A^*\} \\ \{\varepsilon_B^*\} \end{Bmatrix} \quad (A7)$$

where

$$\begin{aligned} [C_A^*] &= \frac{1}{H} \sum_{k=1}^N \int_{z^{k-1}}^{z^k} [C_{AA}]^{-1} dz \\ [C_B^*] &= \frac{1}{H} \sum_{k=1}^N \int_{z^{k-1}}^{z^k} [C_{AA}]^{-1} [C_{AB}] dz \\ [C_D^*] &= \frac{1}{H} \sum_{k=1}^N \int_{z^{k-1}}^{z^k} -[C_{AB}]^T [C_{AA}]^{-1} [C_{AB}] + [C_{BB}] dz \end{aligned} \quad (A8)$$

where N is the number of plies.

Equation (A8) can also be expressed as:

$$\sigma_i^* = \sum_{j=1}^6 C_{ij}^* \varepsilon_j^* \quad (i = 1, 2, \dots, 6) \quad (\text{A9})$$

where C_{ij}^* is the effective stiffness matrix for the RVE after vertical homogenization and the expansion of Equation (A9) is:

$$\begin{Bmatrix} \{\sigma_A^*\} \\ \{\sigma_B^*\} \end{Bmatrix} = \begin{Bmatrix} [C_A^*]^{-1} & [C_A^*]^{-1}[C_B^*] \\ [C_B^*]^T[C_A^*]^{-1} & [C_B^*]^T[C_A^*]^{-1}[C_B^*] + [C_D^*] \end{Bmatrix} \begin{Bmatrix} \{\varepsilon_A^*\} \\ \{\varepsilon_B^*\} \end{Bmatrix} \quad (\text{A10})$$

In the beginning of step 2, the fiber was assumed to be bent, and the RVE was divided into several strips. The number of strips depends upon the wavelength λ ; 20~30 is usually enough for numerical calculation.

In every strip, note that the stiffness C_{ij}^* should be renewed according to the different angle ϕ :

$$C_{ij}^* \Leftarrow T_\phi^{-1} C_{ij}^* T_\phi^{-T} \quad (\text{A11})$$

$$T_\phi = \begin{bmatrix} \cos^2 \phi & 0 & \sin^2 \phi & 0 & 2 \cos \phi \sin \phi & 0 \\ 0 & 1 & 0 & 0 & 0 & 0 \\ \sin^2 \phi & 0 & \cos^2 \phi & 0 & -2 \cos \phi \sin \phi & 0 \\ 0 & 0 & 0 & \cos \phi & 0 & -\sin \phi \\ -\cos \phi \sin \phi & 0 & \cos \phi \sin \phi & 0 & \cos^2 \phi - \sin^2 \phi & 0 \\ 0 & 0 & 0 & \sin \phi & 0 & \cos \phi \end{bmatrix} \quad (\text{A12})$$

where

For the horizontal homogenization, it is assumed that the stresses $\sigma_{xx}^*, \tau_{xy}^*, \tau_{zx}^*$ and strains $\varepsilon_{yy}^*, \varepsilon_{zz}^*, \varepsilon_{yz}^*$ of each strip are continuously uniform across the strip interfaces ($\sigma_{xx}^* = \sigma_{xx}^{**}, \tau_{xy}^* = \tau_{xy}^{**}, \tau_{zx}^* = \tau_{zx}^{**}, \varepsilon_{yy}^* = \varepsilon_{yy}^{**}, \varepsilon_{zz}^* = \varepsilon_{zz}^{**}, \varepsilon_{yz}^* = \varepsilon_{yz}^{**}$). The constitutive relation for a strip can also be rewritten as:

$$\begin{Bmatrix} \{\sigma_E^{**}\} \\ \{\sigma_F^{**}\} \end{Bmatrix} = \begin{Bmatrix} [C_{EE}^*] & [C_{EF}^*] \\ [C_{EF}^*]^T & [C_{FF}^*] \end{Bmatrix} \begin{Bmatrix} \{\varepsilon_E^{**}\} \\ \{\varepsilon_F^{**}\} \end{Bmatrix} \quad (\text{A13})$$

where the superscript ** denotes the effective quantities for the RVE. The other symbols represent:

$$\begin{aligned} \{\sigma_E^{**}\} &= \{\sigma_{xx}^{**} \ \tau_{zx}^{**} \ \tau_{xy}^{**}\}^T, \quad \{\sigma_F^{**}\} = \{\sigma_{yy}^{**} \ \sigma_{zz}^{**} \ \tau_{yz}^{**}\}^T \\ \{\varepsilon_E^{**}\} &= \{\varepsilon_{xx}^{**} \ \gamma_{zx}^{**} \ \gamma_{xy}^{**}\}^T, \quad \{\varepsilon_F^{**}\} = \{\varepsilon_{yy}^{**} \ \varepsilon_{zz}^{**} \ \gamma_{yz}^{**}\}^T \end{aligned} \quad (\text{A14})$$

$$[C_{EE}^*] = \begin{bmatrix} C_{11}^* & C_{15}^* & C_{16}^* \\ C_{15}^* & C_{55}^* & C_{56}^* \\ C_{16}^* & C_{56}^* & C_{66}^* \end{bmatrix}, \quad [C_{EF}^*] = \begin{bmatrix} C_{12}^* & C_{13}^* & C_{14}^* \\ C_{25}^* & C_{35}^* & C_{45}^* \\ C_{26}^* & C_{36}^* & C_{46}^* \end{bmatrix}, \quad [C_{FF}^*] = \begin{bmatrix} C_{22}^* & C_{23}^* & C_{24}^* \\ C_{23}^* & C_{33}^* & C_{34}^* \\ C_{24}^* & C_{34}^* & C_{44}^* \end{bmatrix} \quad (\text{A15})$$

The averages of $\{\sigma_D^*\}$ and $\{\varepsilon_C^*\}$, i.e., $\{\sigma_D^{**}\}$ and $\{\varepsilon_C^{**}\}$ for the homogenized RVE, can also be given by:

$$\begin{Bmatrix} \{\varepsilon_E^{**}\} \\ \{\sigma_F^{**}\} \end{Bmatrix} = \begin{Bmatrix} [C_E^{**}] - [C_F^{**}] \\ [C_F^{**}]^T [C_G^{**}] \end{Bmatrix} \begin{Bmatrix} \{\sigma_E^{**}\} \\ \{\varepsilon_F^{**}\} \end{Bmatrix} \quad (\text{A16})$$

where

$$\begin{aligned} [C_E^{**}] &= \frac{1}{\lambda} \int_{-\lambda/2}^{\lambda/2} [C_{EE}^*]^{-1} dx \\ [C_F^{**}] &= \frac{1}{\lambda} \int_{-\lambda/2}^{\lambda/2} [C_{EE}^*]^{-1} [C_{EF}^*] dx \\ [C_G^{**}] &= \frac{1}{\lambda} \int_{-\lambda/2}^{\lambda/2} (-[C_{EF}^*]^T [C_{EE}^*]^{-1} [C_{EF}^*] + [C_{FF}^*]) dx \end{aligned} \quad (\text{A17})$$

Equation (A16) can also be expressed as:

$$\sigma_i^{**} = \sum_{j=1}^6 C_{ij}^{**} \varepsilon_j^{**} \quad (i = 1, 2, \dots, 6) \quad (\text{A18})$$

where C_{ij}^{**} is the effective stiffness for the RVE after horizontal homogenization and the expansion of equation (A18) is:

$$\begin{Bmatrix} \{\sigma_E^{**}\} \\ \{\sigma_F^{**}\} \end{Bmatrix} = \begin{Bmatrix} [C_E^{**}]^{-1} & [C_E^{**}]^{-1}[C_F^{**}] \\ [C_F^{**}]^T[C_E^{**}]^{-1} & [C_F^{**}]^T[C_E^{**}]^{-1}[C_F^{**}] + [C_G^{**}] \end{Bmatrix} \begin{Bmatrix} \{\varepsilon_E^{**}\} \\ \{\varepsilon_F^{**}\} \end{Bmatrix} \quad (\text{A19})$$

References

- Hallander, P.; Akermo, M.; Mattei, C.; Petersson, M.; Nyman, T. An experimental study of mechanisms behind wrinkle development during forming of composite laminates. *Compos. Part A Appl. Sci. Manuf.* **2013**, *50*, 54–64. [CrossRef]
- Sorrentino, L.; Bellini, C. Potentiality of hot drape forming to produce complex shape parts in composite material. *Int. J. Adv. Manuf. Technol.* **2016**, *85*, 945–954. [CrossRef]
- Farnand, K.; Zobeiry, N.; Poursartip, A.; Fernlund, G. Micro-level mechanisms of fiber waviness and wrinkling during hot drape forming of unidirectional prepreg composites. *Compos. Part A Appl. Sci. Manuf.* **2017**, *103*, 168–177. [CrossRef]
- Jochum, C.; Grandidier, J.C.; Smaali, M. Proposal for a long-fiber microbuckling scenario during the cure of a thermosetting matrix. *Compos. Part A Appl. Sci. Manuf.* **2008**, *39*, 19–28. [CrossRef]
- Potter, K.; Khan, B.; Wisnom, M.; Bell, T.; Stevens, J. Variability, fiber waviness and misalignment in the determination of the properties of composite materials and structures. *Compos. Part A Appl. Sci. Manuf.* **2008**, *39*, 1343–1354. [CrossRef]
- Alshahrani, H.; Hojjati, M. Experimental and numerical investigations on formability of out-of-autoclave thermoset prepreg using a double diaphragm process. *Compos. Part A Appl. Sci. Manuf.* **2017**, *101*, 199–214. [CrossRef]
- Lightfoot, J.S.; Wisnom, M.R.; Potter, K. Defects in woven preforms: Formation mechanisms and the effects of laminate design and layup protocol. *Compos. Part A Appl. Sci. Manuf.* **2013**, *51*, 99–107. [CrossRef]
- Weber, T.A.; Englehard, M.; Arent, J.C.; Hausmann, J. An experimental characterization of wrinkling generated during prepreg autoclave manufacturing using caul plates. *J. Compos. Mater.* **2019**, *53*, 3757–3773. [CrossRef]
- Nebe, M. In *Situ Characterization Methodology for the Design and Analysis of Composite Pressure Vessels*; Springer Fachmedien: Wiesbaden, Germany, 2022; Available online: <https://link.springer.com/10.1007/978-3-658-35797-9> (accessed on 24 February 2022). [CrossRef]
- Mukhopadhyay, S.; Jones, M.I.; Hallett, S.R. Compressive failure of laminates containing an embedded wrinkle: Experimental and numerical study. *Compos. Part A Appl. Sci. Manuf.* **2015**, *73*, 132–142. [CrossRef]
- Xie, N.B.; Smith, R.A.; Mukhopadhyay, S.; Hallett, S.R. A numerical study on the influence of composite wrinkle defect geometry on compressive strength. *Mater. Des.* **2018**, *140*, 7–20. [CrossRef]
- Wu, C.J.; Gu, Y.Z.; Luo, L.; Xu, P.; Wang, S.K.; Li, M.; Zhang, Z.G. Influences of in-plane and out-of-plane fiber waviness on mechanical properties of carbon fiber composite laminate. *J. Reinf. Plast. Compos.* **2018**, *37*, 877–891. [CrossRef]
- Bloom, L.D.; Wang, J.; Potter, K.D. Damage progression and defect sensitivity: An experimental study of representative wrinkles in tension. *Compos. Part B Eng.* **2013**, *45*, 449–458. [CrossRef]
- Mukhopadhyay, S.; Jones, M.I.; Hallett, S.R. Tensile failure of laminates containing an embedded wrinkle; numerical and experimental study. *Compos. Part A Appl. Sci. Manuf.* **2015**, *77*, 219–228. [CrossRef]
- Mukhopadhyay, S.; Nixon-Pearson, O.J.; Hallett, S.R. An experimental and numerical study on fatigue damage development in laminates containing embedded wrinkle defects. *Int. J. Fatigue* **2018**, *107*, 1–12. [CrossRef]
- Elhajjar, R.F.; Petersen, D.R. Gaussian function characterization of unnotched tension behavior in a carbon/epoxy composite containing localized fiber waviness. *Compos. Struct.* **2011**, *93*, 2400–2408. [CrossRef]
- Riddle, T.; Cairns, D.; Nelson, J. Characterization of manufacturing defects common to composite wind turbine blades: Flaw characterization. In Proceedings of the 52nd, AIAA/ASME/ASCE/AHS/ASC Structures, Structural Dynamics and Materials Conference, Denver, CO, USA, 4–7 April 2011.
- Riddle, T.W.; Cairns, D.S.; Nelson, J.W. Effects of Defects Part A: Treatment of Manufacturing Defects as Uncertainty Variables in a Wind Blade Probabilistic Design Framework. In Proceedings of the 32nd ASME Wind Energy Symposium, National Harbor, MD, USA, 13–17 January 2014.
- Pain, D.; Drinkwater, B.W. Detection of fibre waviness using ultrasonic array scattering data. *J. Nondestruct. Eval.* **2013**, *32*, 215–227. [CrossRef]
- Nelson, L.J.; Smith, R.A.; Mienzakowski, M. Ply-orientation measurements in composites using structure-tensor analysis of volumetric ultrasonic data. *Compos. Part A Appl. Sci. Manuf.* **2018**, *104*, 108–119. [CrossRef]
- Nelson, L.J.; Smith, R.A. Fibre direction and stacking sequence measurement in carbon fibre composites using Radon transforms of ultrasonic data. *Compos. Part A Appl. Sci. Manuf.* **2018**, *118*, 1–8. [CrossRef]

22. Smith, R.A.; Nelson, L.J.; Mienczakowski, M.J.; Wilcox, P.D. Ultrasonic analytic-signal responses from polymer-matrix composite laminates. *IEEE Trans. Ultrason. Ferroelectr. Freq. Control* **2018**, *65*, 231–243. [\[CrossRef\]](#)
23. Ambrozinski, L.; Mrowka, J.; O'Donnell, M.; Pelivanov, I. Detection and imaging of local ply angle in carbon fiber reinforced plastics using laser ultrasound and tilt filter processing. *Compos. Part A Appl. Sci. Manuf.* **2019**, *126*, 105581. [\[CrossRef\]](#)
24. Li, Z.C.; Zhou, L.C.; Pei, Y.M. Microwave near-field and far-field imaging of composite plate with hat stiffeners. *Compos. Part B Eng.* **2019**, *161*, 87–95. [\[CrossRef\]](#)
25. Sutcliffe, M.P.F.; Lemanski, S.L.; Scott, A.E. Measurement of fibre waviness in industrial composite components. *Compos. Sci. Technol.* **2012**, *72*, 2016–2023. [\[CrossRef\]](#)
26. Elhajjar, R.F.; Shams, S.S. A new method for limit point determination in composite materials containing defects using image correlation. *Compos. Sci. Technol.* **2016**, *122*, 140–148. [\[CrossRef\]](#)
27. Takeda, T. Micromechanics model for three-dimensional effective elastic properties of composite laminates with ply wrinkles. *Compos. Struct.* **2018**, *189*, 419–427. [\[CrossRef\]](#)
28. Chou, P.C.; Carleone, J.; Hsu, C.M. Elastic constants of layered media. *J. Compos. Mater.* **1972**, *6*, 80–93. [\[CrossRef\]](#)
29. Sun, C.T.; Li, S. Three-dimensional effective elastic constants for thick laminates. *J. Compos. Mater.* **1988**, *22*, 629–639. [\[CrossRef\]](#)
30. Whitcomb, J.; Noh, J. Concise derivation of formulas for 3D sublaminat homogenization. *J. Compos. Mater.* **2000**, *34*, 522–535. [\[CrossRef\]](#)
31. Sandhu, A.; Reinartz, A.; Dodwell, T.J. A Bayesian framework for assessing the strength distribution of composite structures with random defects. *Compos. Struct.* **2018**, *205*, 58–68. [\[CrossRef\]](#)
32. Felipe-Sesé, L.; López-Alba, E.; Siegmund, P.; Díaz, F.A. Integration of fringe projection and two-dimensional digital image correlation for three-dimensional displacements measurements. *Opt. Eng.* **2016**, *55*, 121711. [\[CrossRef\]](#)
33. Wu, Z.; Guo, W.; Pan, B.; Kemao, Q.; Zhang, Q. A DIC-assisted fringe projection profilometry for high-speed 3D shape, displacement and deformation measurement of textured surfaces. *Opt. Lasers Eng.* **2021**, *142*, 106614. [\[CrossRef\]](#)

Disclaimer/Publisher's Note: The statements, opinions and data contained in all publications are solely those of the individual author(s) and contributor(s) and not of MDPI and/or the editor(s). MDPI and/or the editor(s) disclaim responsibility for any injury to people or property resulting from any ideas, methods, instructions or products referred to in the content.